

The quantum metric of electrons with spin-momentum locking

Giacomo Sala,^{1,*} Maria Teresa Mercaldo,² Klevis Domi,¹ Stefano Gariglio,¹
Mario Cuoco,³ Carmine Ortix,^{2,*} Andrea D. Caviglia^{1,*}

¹Department of Quantum Matter Physics, University of Geneva, Geneva, Switzerland

²Dipartimento di Fisica ‘E. R. Caianiello’, Università di Salerno, Fisciano, Italy

³CNR-SPIN c/o Università di Salerno, Fisciano, Italy

*To whom correspondence should be addressed;

E-mail: giacomo.sala@unige.ch, cortix@unisa.it, andrea.caviglia@unige.ch

Quantum materials are characterized by electromagnetic responses intrinsically linked to the geometry and topology of the electronic wavefunctions. These properties are encoded in the quantum metric and Berry curvature. While Berry curvature-mediated transport effects such as the anomalous and nonlinear Hall effects have been identified in several magnetic and nonmagnetic systems, quantum metric-induced transport phenomena remain limited to topological antiferromagnets. Here we show that spin-momentum locking – a general characteristic of the electronic states at surfaces and interfaces of spin-orbit coupled materials – leads to a nontrivial quantum metric. This metric activates a nonlinear in-plane magnetoresistance that we measure and electrically control in 111-oriented LaAlO₃/SrTiO₃ interfaces. These findings demonstrate the existence of quantum metric effects in a vast class of materials and provide new strategies to design functionalities based on the quantum

geometry.

Nonlinear electronic responses can reveal physical properties that are out of the reach of linear probes (*1*). For example, the anomalous Hall effect senses the Berry curvature of magnetic materials (*2, 3*). In comparison, its nonlinear, second-order counterpart can exist even in the presence of time-reversal symmetry in noncentrosymmetric and nonmagnetic materials and provides information on closely-related geometric quantities: the Berry curvature dipole (*4–8*) and the Berry curvature triple (*9*).

Nonlinear electronic responses can also manifest themselves as a nonreciprocal magnetoresistance, which was conventionally associated with disorder (*1*). However, recent works have identified an intrinsic nonlinear magnetoresistance driven by the quantum metric of electronic wavefunctions (*10, 11*). The quantum metric $g = \Re(G)$ corresponds to the real part of the quantum geometric tensor G and, together with the Berry curvature $\Omega = -2\Im(G)$, defines the geometrical and topological characteristics of quantum systems (*12–14*). Despite the profound implications of the quantum metric for several physical phenomena (*14–18*), its experimental observations remain scarce (*19–25*) and, in metallic systems, limited to topological antiferromagnets (*26, 27*).

Here, we theoretically predict and experimentally demonstrate that a condensed-matter phenomenon as fundamental (*28, 29*) and technologically relevant (*30, 31*) as the spin-momentum locking of electronic states at surfaces and interfaces of spin-orbit coupled materials is endowed with a nontrivial quantum metric. This intrinsic geometrical feature activates a nonlinear and nonreciprocal in-plane magnetoresistance that we use to provide evidence of the quantum metric at 111-oriented $\text{LaAlO}_3/\text{SrTiO}_3$ interfaces. Our findings and the abundance of materials with spin-momentum locked electronic bands broaden the significance of the quantum metric in condensed matter and opens up a whole line of possibilities to explore the quantum geometry in a variety of systems (*14*).

Quantum metric of spin-momentum locked electronic bands The direct relation between the spin-momentum locking and the quantum metric can be found by considering the general case of a single pair of Kramers' related bands with parabolic dispersion that are shifted in momentum space by a Rashba-like linear term $\alpha_R(\mathbf{z} \times \mathbf{k}) \cdot \boldsymbol{\sigma}$ (29). Here, \mathbf{z} is the direction normal to the surface or interface of interest and α_R is the Rashba parameter. The linear coupling between the crystalline momentum \mathbf{k} and the electron spins $\boldsymbol{\sigma}$ leads to helical spin textures (Fig. 1A) that are characterized by the complete absence of the Berry curvature (6). Nevertheless, we find here that the quantum metric of spin-locked electronic bands is generally finite. As shown in Fig. 1B, the metric diagonal components g_{xx} and g_{yy} vanish only along the $k_y = 0$ and $k_x = 0$ lines, respectively, and possess a singular point at the time-reversal invariant momentum $\mathbf{k} = 0$. The band-energy normalized quantum metrics (BNQM, also known as Berry connection polarizabilities) of the spin-split bands cancel each other at the same crystal momentum. However, in the region of momenta populated by a single spin band the BNQM is finite. This implies that the dipole density components Λ_{xxx} and Λ_{yyy} of the BNQM governing the longitudinal nonlinear conductivities feature alternating positive and negative hotspots with a characteristic quadrupolar profile in momentum space (Fig. 1C and Supplementary Material). In the absence of magnetic fields, i.e., in time-reversal invariant conditions, the integrated dipole components vanish and so does the nonlinear response associated with the quantum metric (10). We consider next the effect of a planar magnetic field B , which, without loss of generality, we set along the y direction. The Kramers' doublet at $\mathbf{k} \neq 0$ is now split, but a mirror symmetry-protected double degeneracy still occurs on the residual mirror symmetric line $k_y = 0$. The ensuing distortion of the spin-split bands is accompanied by an analogous change of the spin textures, which still preserve a mirror-symmetric arrangement. Thus, the only effect of the magnetic field on the quantum metric is a simple shift of its singular point and lines of zeros. However, the consequences for the dipole of the BNQM are completely different. In the dis-

torted annulus between the two Fermi lines of the spin-split bands, the BNQM dipoles lose their quadrupolar profile. As a result, the integrated dipole component Λ_{xxx} governing the nonlinear response perpendicular to the magnetic field becomes finite. Its magnitude increases linearly with B for small magnetic fields and diverges at the critical field B_c at which the Fermi lines of the two split-spin bands intersect each other on the band degeneracy point (Supplementary Material). For magnetic fields much larger than B_c , the nonlinear response becomes again vanishingly small.

The spin-momentum locking is therefore endowed with a nontrivial quantum metric that exists in time-reversal symmetric conditions. A planar magnetic field lifts this symmetry and activates a nonlinear in-plane magnetoresistance that can be thus used as a probing tool of the quantum metric. We call this effect quantum metric magnetoresistance (QMMR). Importantly, the BNQM dipole component Λ_{yyy} regulating the nonlinear conductivity parallel to the applied magnetic field remains overall zero, which implies the absence of a nonlinear magnetoresistance in the direction of B . This features makes the QMMR similar to the semiclassical Drude-like bilinear magnetoelectric resistance (BMER) first unveiled at the surfaces of three-dimensional topological insulators (32), but with one important difference. The BMER of the Rashba spin-split bands is strictly zero for magnetic fields smaller than B_c (Supplementary Material and Ref. (33)), thus making the nonlinear in-plane magnetoresistance at small fields completely determined by the BNQM.

Nonlinear magnetotransport To probe this quantum magnetotransport effect, we consider the two-dimensional electron gas at the 111-oriented $\text{LaAlO}_3/\text{SrTiO}_3$ interface (Fig. 2A). The heterostructures are synthesized by pulsed laser deposition and lithographically patterned into Hall bars oriented along the two principal in-plane crystallographic directions: the $[\bar{1}10]$ (x) and the $[\bar{1}\bar{1}2]$ (y) axis (Fig. 2B and Supplementary Material). The sheet conductivity of the electron

gas is controlled by an electrostatic field effect in a back-gate geometry that tunes the carrier density and mobility (Fig. 2C) (34, 35). The combination of spin-orbit coupling and orbital degrees of freedom associated with the t_{2g} electrons of Ti atoms leads to three Kramers' related pairs of Rashba bands, enabling a gate-induced Lifshitz transition from one- to multi-carrier transport (Fig. 2D) (36–38). The Rashba effect endows all three band pairs with the quantum metric and BNQM dipoles discussed above. However, the nonlinear magnetotransport driven by the quantum metric is expected to be always dominated by one pair of bands only. This is because the critical magnetic field B_c depends strongly on the band filling and is of the order of a few Teslas when the chemical potential is close to the band bottom of one of the Kramers' pairs (Supplementary Material). Put differently, at intermediate fields only low-filled Rashba bands yield a sizable QMMR.

Figure 3 showcases the electronic response of the 2D electron gas as a function of the planar magnetic field oriented along the $[\bar{1}10]$ direction. At fields well below 3 T, the first harmonic transverse resistance R_{xy}^ω increases linearly with the magnetic field strength, which is compatible with a small out-of-plane misalignment of the field (Fig. 3A). However, R_{xy}^ω increases sharply above a magnetic field threshold modulated by the back gate. This sudden onset can be attributed to the anomalous planar Hall effect appearing in systems without mirror symmetries (39). We note that, although the magnetic field along the $[\bar{1}10]$ direction leaves a residual mirror symmetry on the triangular Ti atoms net, the antiferrodistortive octahedron rotations of the oxygen atoms and the formation of domain patterns at the cubic-to-tetragonal transition of SrTiO_3 make our system mirror-free independently of the magnetic field direction. This then leads to the emergence of Berry curvature hotspots when the avoided level crossing at B_c enters the Fermi surface annulus (6). The appearance of the anomalous planar Hall effect at fields of a few Teslas thus confirms that the critical magnetic field B_c is experimentally accessible and that the chemical potential lies close to the bottom of one of the Kramers' pairs.

At magnetic field strengths $B \geq 2$ T, we also observe a nonlinear and field-antisymmetric in-plane magnetoresistance $R_{yyy}^{2\omega, \text{asym}}$ (Fig. 3B) that is strongly suppressed when the magnetic field is collinear with the current (Fig. 3C). Sweeping the gate voltage allows us to tune $R_{yyy}^{2\omega, \text{asym}}$ and explore its dependence on the band filling. As shown in Fig. 3E, the nonlinear magnetoconductivity $\sigma_{yyy}^{2\omega} = J_y^{2\omega}/(E_y^\omega)^2$ associated with $R_{yyy}^{2\omega, \text{asym}}$ vanishes in the low conductivity region and sharply emerges at a threshold $\sigma_{yy} = J_y^\omega/E_y^\omega \simeq 6$ mS, similar to the anomalous planar Hall conductivity $\sigma_{xy}^\omega = J_x^\omega/E_y^\omega$ (Fig. 3D). Measurements of the ordinary Hall effect reveal that a transition from one to two-carrier transport occurs at this threshold conductivity (Fig. 3F, Supplementary Material) (35, 37). This finding indicates that the enhancement of the nonlinear response practically coincides with the filling of the second pair of Kramers' related bands. All together, these observations demonstrate the existence of a nonlinear longitudinal electronic response that fulfils the requirements of the BNQM-driven magnetotransport. We note that the field-symmetric counterpart of $R_{yyy}^{2\omega, \text{asym}}$ cannot originate from the quantum metric but derives from nonlinear skew scattering and side-jump contributions that exist also in the presence of time-reversal symmetry (Supplementary Material) (8, 40).

Quantum metric nonlinear magnetoresistance Our experimental observations cannot be attributed to thermal effects, nonohmic contacts, and capacitive or inductive coupling (Supplementary Material). Instead, the nonlinear in-plane magnetoresistance is compatible with the QMMR of Rashba spin-split bands and the BMER. We note that, because of hexagonal warping effects in 111-oriented heterostructures, the BMER can be finite not only for magnetic field strengths larger than the critical magnetic field but also for $B < B_c$ (33). The observation of a quantum metric-induced nonlinear transport, therefore, requires to disentangle the QMMR from the BMER. We use to this aim the fact that the QMMR and BMER contributions to the total nonlinear magnetoresistance can be parsed thanks to their different dependence on the

electronic scattering time τ (10). The latter can be controlled via the gate tunability of the sheet conductance or by varying temperature. While the QMMR contribution σ_{qm} is intrinsic in origin and scales as τ^0 , the BMER grows with the square of the scattering time, i.e., as $\sim \tau^2$. Since the mobility is linear in the band-resolved relaxation time, we can equivalently consider the dependence of the nonlinear conductivity on the mobility μ_2 of the second Kramers pair of bands. As shown in Fig. 4B, this scaling analysis allows us to pinpoint the two effects in the conductivity region in which the carrier density n_2 is constant (27). We find that both the QMMR and the BMER conductivities change nonmonotonically with the magnetic field (Fig. 4C), in agreement with our theory calculations based on a Rashba two-dimensional electron gas with an additional trigonal warping (Fig. 4D and Supplementary Material). Note that the theoretical analysis predicts an opposite sign for the QMMR and BMER, which also matches our experimental observation. We can then conclude that the Rashba electron gas at the 111-oriented $\text{LaAlO}_3/\text{SrTiO}_3$ interface features a nonlinear magnetoresistance driven by a quantum metric contribution that is three orders of magnitude larger than that reported for 2D topological antiferromagnets at a similar temperature (27).

We have finally performed a similar scaling analysis of the anomalous planar Hall resistance to account for the presence of disorder-mediated effects beside the intrinsic Berry curvature-induced contribution. The linear dependence of the anomalous planar Hall conductivity on the mobility μ_2 (Fig. 4A) demonstrates the existence of a skew scattering contribution σ_{sk} that is absent in a rotational symmetric Rashba two-dimensional electron system (41) but is activated by the nonvanishing Berry curvature triple due to hexagonal warping effects (9). In addition, the τ^0 term due to the combined action of side-jump and intrinsic Berry curvature varies non-monotonically as the magnetic field is increased. This behavior is correctly captured by a theory calculation of the Berry curvature-mediated anomalous planar Hall response (Fig. 4D), which thus proves that the intrinsic contribution dominates the τ -independent anomalous planar Hall

conductivity. Therefore, the intrinsic contributions to the anomalous planar Hall effect and nonlinear in-plane magnetoresistance provide us with direct access to the Berry curvature and the quantum metric of the 111-oriented $\text{LaAlO}_3/\text{SrTiO}_3$ interface and allow us to probe its full quantum geometric tensor. This unique property marks the difference of $\text{LaAlO}_3/\text{SrTiO}_3$ with respect to \mathcal{PT} -symmetric materials like topological antiferromagnets (26, 27), where the quantum geometric tensor is purely real and accessible only via the nonlinear response.

Outlook The analysis of the conductivity dependence on the scattering time allowed us to identify the intrinsic contribution of the quantum metric and Berry curvature to the electronic magnetotransport. Our findings do not only demonstrate the existence of a nontrivial quantum metric associated with the spin-momentum locking but unlock new directions for investigating and functionalizing the quantum geometry in a vast class of nonmagnetic materials. The QMMR is not limited to oxide heterostructures (42, 43) but is expected for all materials with spin-locked electronic bands such as semiconductors (28, 44–46), surface states of heavy metals (47), and magnetic and nonmagnetic interfaces (28, 29, 48). Besides magnetotransport, the quantum metric of the spin-momentum locking is, in principle, accessible to THz photocurrents and spectroscopic tools in time-reversal symmetric conditions (49, 50). In a technological perspective, integrating the spin-momentum locking with magnetic and ferroelectric thin films could lead to the on-demand, reversible, and nonvolatile control of the physical effects emerging from the quantum metric. Moreover, combining spintronics with the quantum metric may reveal unforeseen disorder-free mechanisms to interconvert charge and spin-orbital currents (28, 29, 51). This study discloses therefore a whole range of possibilities to harness quantum metric effects in condensed matter and ultimately inspire technologies based on the geometry of the electronic wavefunctions.

References

1. Y. Tokura, N. Nagaosa, *Nat. Commun.* **9**, 3740 (2018).
2. D. Xiao, M.-C. Chang, Q. Niu, *Rev. Mod. Phys.* **82**, 1959 (2010).
3. N. Nagaosa, J. Sinova, S. Onoda, A. H. MacDonald, N. P. Ong, *Rev. Mod. Phys.* **82**, 1539 (2010).
4. I. Sodemann, L. Fu, *Phys. Rev. Lett.* **115**, 216806 (2015).
5. Q. Ma, *et al.*, *Nature* **565**, 337 (2019).
6. E. Lesne, *et al.*, *Nat. Mater.* **22**, 576 (2023).
7. Z. Z. Du, H.-Z. Lu, X. C. Xie, *Nat. Rev. Phys.* **3**, 744 (2021).
8. C. Ortix, *Adv. Quantum Technol.* **4**, 1 (2021).
9. P. Makushko, *et al.*, *Nat. Electron.* **7**, 207 (2024).
10. D. Kaplan, T. Holder, B. Yan, *Phys. Rev. Lett.* **132**, 026301 (2024).
11. K. Das, S. Lahiri, R. B. Atencia, D. Culcer, A. Agarwal, *Phys. Rev. B* **108**, L201405 (2023).
12. J. P. Provost, G. Vallee, *Commun. Math. Phys.* **76**, 289 (1980).
13. R. Cheng, *arXiv 1012.1337* pp. 1–9 (2010).
14. P. Torma, *Phys. Rev. Lett.* **131**, 240001 (2023).
15. R. Resta, *Eur. Phys. J. B* **79**, 121 (2011).
16. S. Peotta, P. Törmä, *Nat. Commun.* **6**, 8944 (2015).

17. E. Rossi, *Curr. Opin. Solid State Mater. Sci.* **25**, 100952 (2021).
18. K.-E. Huhtinen, J. Herzog-Arbeitman, A. Chew, B. A. Bernevig, P. Törmä, *Phys. Rev. B* **106**, 014518 (2022).
19. X. Tan, *et al.*, *Phys. Rev. Lett.* **122**, 210401 (2019).
20. A. Gianfrate, *et al.*, *Nature* **578**, 381 (2020).
21. M. Yu, *et al.*, *Natl. Sci. Rev.* **7**, 254 (2020).
22. J. Ren, *et al.*, *Nat. Commun.* **12**, 689 (2021).
23. Q. Liao, *et al.*, *Phys. Rev. Lett.* **127**, 107402 (2021).
24. H. Tian, *et al.*, *Nature* **614**, 440 (2023).
25. C.-R. Yi, *et al.*, *Phys. Rev. Res.* **5**, L032016 (2023).
26. A. Gao, *et al.*, *Science* (80-.). **381**, 181 (2023).
27. N. Wang, *et al.*, *Nature* **621**, 487 (2023).
28. C. H. Li, *et al.*, *Nat. Nanotechnol.* **9**, 218 (2014).
29. G. Bihlmayer, P. Noël, D. V. Vyalikh, E. V. Chulkov, A. Manchon, *Nat. Rev. Phys.* **4**, 642 (2022).
30. S. Manipatruni, *et al.*, *Nature* **565**, 35 (2019).
31. P. Noël, *et al.*, *Nature* **580**, 483 (2020).
32. P. He, *et al.*, *Nat. Phys.* **14**, 495 (2018).
33. G. Tuvia, *et al.*, *Phys. Rev. Lett.* **132**, 146301 (2024).

34. A. D. Caviglia, *et al.*, *Nature* **456**, 624 (2008).
35. A. M. Monteiro, *et al.*, *Phys. Rev. B* **99**, 201102 (2019).
36. T. C. Rödel, *et al.*, *Phys. Rev. Appl.* **1**, 1 (2014).
37. U. Khanna, *et al.*, *Phys. Rev. Lett.* **123**, 036805 (2019).
38. M. Diez, *et al.*, *Phys. Rev. Lett.* **115**, 016803 (2015).
39. R. Battilomo, N. Scopigno, C. Ortix, *Phys. Rev. Res.* **3**, L012006 (2021).
40. Z. Z. Du, C. M. Wang, S. Li, H.-Z. Lu, X. C. Xie, *Nat. Commun.* **10**, 3047 (2019).
41. M. Borunda, *et al.*, *Phys. Rev. Lett.* **99**, 066604 (2007).
42. A. Ohtomo, H. Y. Hwang, *Nature* **427**, 423 (2004).
43. L. M. Vicente-Arche, *et al.*, *Adv. Mater.* **33**, 1 (2021).
44. J. Nitta, T. Akazaki, H. Takayanagi, T. Enoki, *Phys. Rev. Lett.* **78**, 1335 (1997).
45. T. Ideue, *et al.*, *Nat. Phys.* **13**, 578 (2017).
46. Y. Li, *et al.*, *Nat. Commun.* **12**, 540 (2021).
47. C. R. Ast, *et al.*, *Phys. Rev. Lett.* **98**, 186807 (2007).
48. J. C. R. Sánchez, *et al.*, *Nat. Commun.* **4**, 2944 (2013).
49. J. Ahn, G.-Y. Guo, N. Nagaosa, *Phys. Rev. X* **10**, 041041 (2020).
50. Q. Ma, R. Krishna Kumar, S.-Y. Xu, F. H. L. Koppens, J. C. W. Song, *Nat. Rev. Phys.* **5**, 170 (2023).

51. X. Feng, *et al.*, *arXiv 2402.00532* pp. 1–6 (2024).
52. D. Bures, *Trans. Am. Math. Soc.* **135**, 199 (1969).
53. S. Hikami, A. I. Larkin, Y. Nagaoka, *Prog. Theor. Phys.* **63**, 707 (1980).
54. S. Maekawa, H. Fukuyama, *J. Phys. Soc. Japan* **50**, 2516 (1981).
55. G. Sala, The quantum metric of electrons with spin-momentum locking, <https://doi.org/10.5281/zenodo.10692339> (2024).

Acknowledgments

We thank Jean-Marc Triscone, Marc Gabay, Ajit Srivastava, Edouard Lesne, and Graham Kimbell for fruitful discussions. We thank Marco Lopes and Jean-Luc Lorenzoni for technical support. We thank Alberto Morpurgo and Ignacio Gutiérrez for contributing to the sample fabrication. **Funding** G.S. and A.D.C. acknowledge ERC/SERI, Moore Foundation. M.T.M and M.C. acknowledge support from the EU Horizon 2020 research and innovation program under Grant Agreement No. 964398 (SUPERGATE). M.T.M. and C.O. acknowledge support from the MAECI project "ULTRAQMAT". M.C. acknowledges financial support from PNRR MUR project PE0000023-NQSTI. **Author contributions** G.S. fabricated the oxide heterostructures and the transport devices used in this study. G.S. and K.D. performed the measurements and analyzed the data with the support of S.G.. M.T.M., M.C., and C.O. developed the theoretical model. A.D.C. supervised the experimental work, and C.O. supervised the theoretical work. All authors contributed to writing the manuscript. **Competing interests** The authors declare no competing financial interests. **Data and materials availability** The data that support the findings of this study are available from Zenodo (55) and from the corresponding authors upon reasonable request.

Supplementary materials

Materials and Methods

Supplementary Text

Figs. S1 to S12

References (52-54)

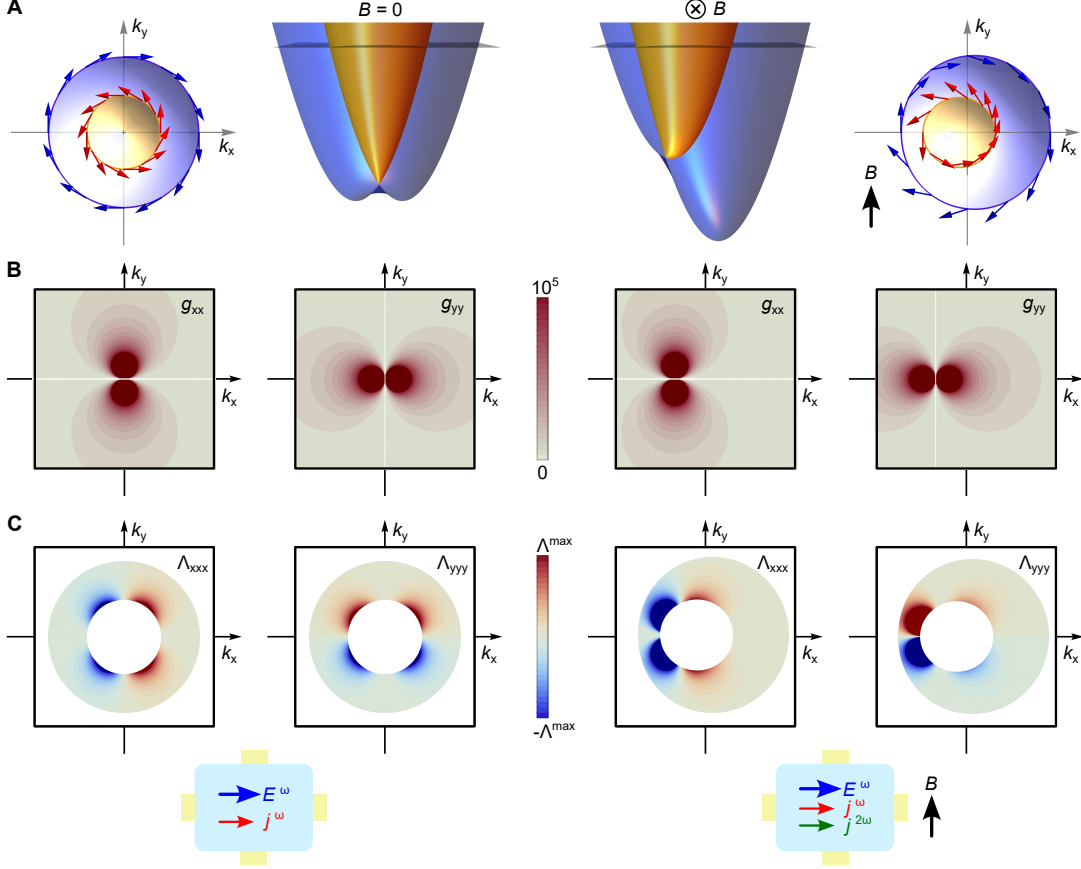


Figure 1: Quantum geometry of 2D Rashba bands. (A) Spin-locked electronic bands induced by the 2D Rashba effect in the absence (left) and presence (right) of a planar magnetic field $B = 0.1E_0$, with E_0 a reference energy (see Supplemental Material). (B) Reciprocal space maps of the diagonal components g_{xx} and g_{yy} of the quantum metric tensor of the Rashba bands at zero and nonzero planar magnetic field. The maps were calculated assuming a Rashba parameter $\alpha_R = 0.4\epsilon_F/k_F$, with ϵ_F and k_F the Fermi energy and Fermi wavevector, respectively. (C) Contour plots of the dipole density components Λ_{xxx} and Λ_{yyy} of the band-normalized quantum metric in the exclusion region between the two Fermi lines. In response to an electric field E^ω , the planar magnetic field activates a nonlinear longitudinal current $j^{2\omega}$ driven by the band-normalized quantum metric.

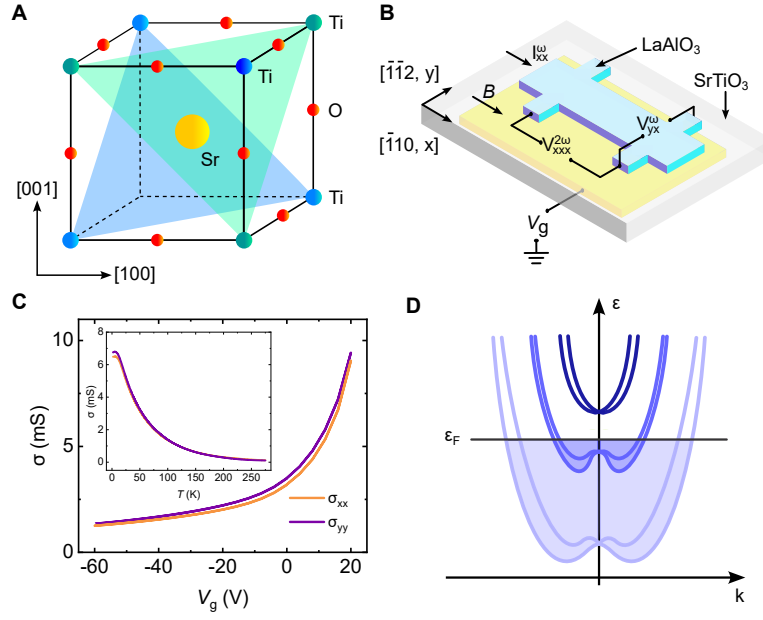


Figure 2: 2D electron gas at the 111-oriented LaAlO₃/SrTiO₃ interface. (A) Crystal structure of SrTiO₃. The shaded triangles identify the {111} planes of Ti atoms. (B) Sketch of the magnetotransport measurements. The transverse and longitudinal first and second harmonic voltages are measured in a Hall bar device while sweeping the magnetic field along the $[\bar{1}\bar{1}0]$ (x) or $[\bar{1}\bar{1}2]$ (y) direction. Two devices with the current path oriented along x and y are measured simultaneously. A variable gate voltage V_g is applied at the back of the sample. (C) Gate voltage and temperature (inset) dependence of the sheet conductivity. (D) Schematic representation of the (exaggerated) Rashba-split electronic bands at the LaAlO₃/SrTiO₃ interface.

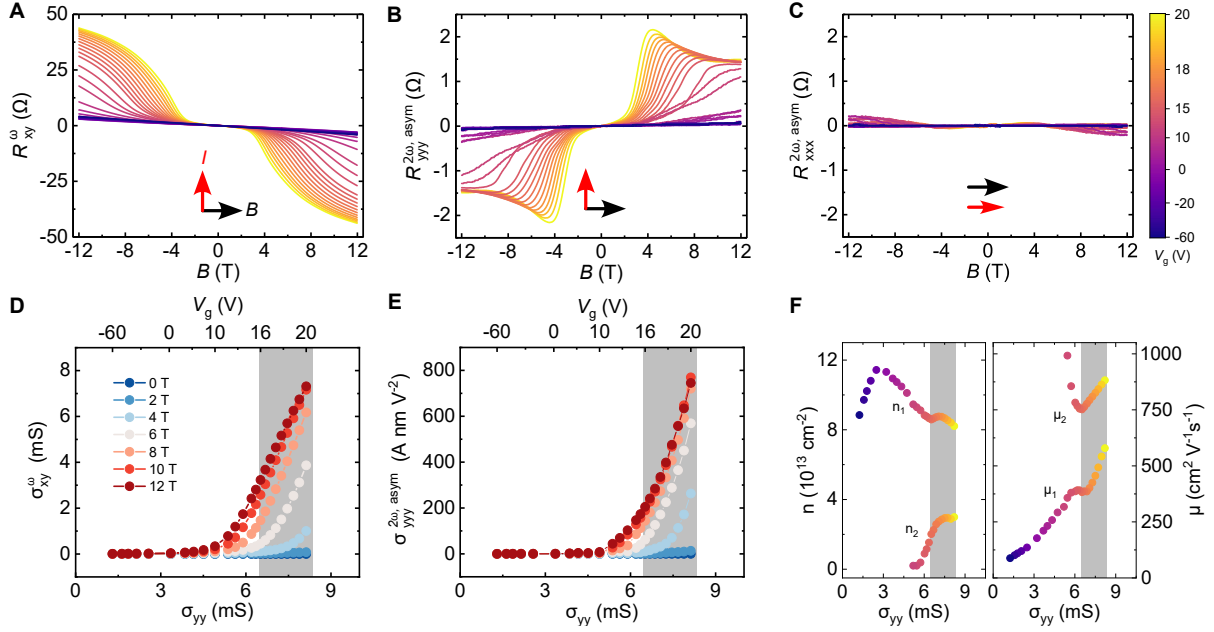


Figure 3: Linear and nonlinear magnetotransport. (A-C) First harmonic transverse and second harmonic longitudinal resistances as a function of the in-plane magnetic field B and gate voltage V_g at a temperature $T = 3$ K. The black and red arrows indicate the direction of B and the electric current I , respectively. The current is applied along the $\bar{1}\bar{1}2$ (y) and $\bar{1}10$ (x) crystallographic directions in A, B and C, respectively. (D) Transverse linear conductivity calculated from A at different magnetic fields as a function of the zero-field longitudinal linear conductivity. (E) The same as D for the longitudinal nonlinear conductivity calculated from B. (F) Two-band electron densities n and mobilities μ at variable V_g and $T = 3$ K. The shaded areas define the conductivity regions considered in Fig. 4.

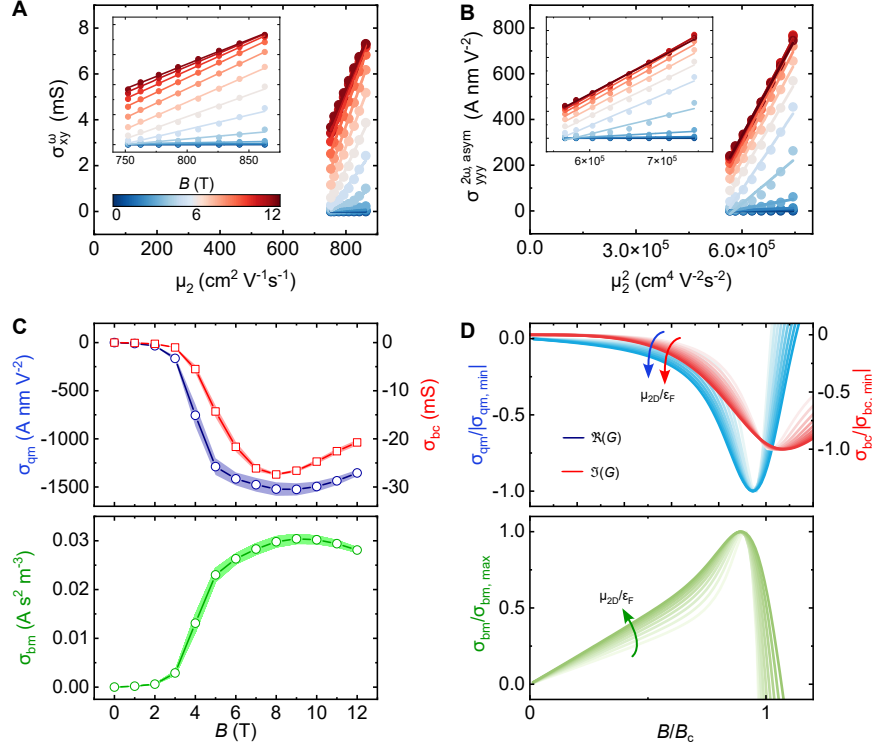


Figure 4: **Probing the full quantum geometric tensor.** (A) Linear transverse conductivity at different magnetic fields as a function of the electron mobility of the second Kramers pair. The lines are linear fits to the data. The inset is a zoom on the data of the main graph. (B) Nonlinear longitudinal conductivity as a function of the square of the electron mobility of the second Kramers pair. (C) Quantum metric (σ_{qm}), Berry curvature (σ_{bc}), and bilinear magnetoelectric (σ_{bm}) conductivities extracted from the fits in A, B as a function of the magnetic field. The shaded areas define the uncertainty of the fits. (D) Predicted magnetic field dependence of the normalized linear conductivity associated with the Berry curvature (σ_{bc}) and normalized nonlinear conductivities due to the quantum metric (σ_{qm}) and bilinear magnetoelectric resistance (σ_{bm}). The color intensity codes the ratio $\mu_{2D}/\epsilon_F = 0.2 - 0.6$ between the chemical potential of the 2D electron gas and the Fermi energy ϵ_F . The magnetic field is normalized to the critical field B_c .